Synergy between Fe and Ni in the optimal performance of (Ni,Fe)OOH catalysts for the oxygen evolution reaction

Hai Xiao[a,b], Hyeyoung Shin[a,b], and William A. Goddard III[a,b,1]

[a]Materials and Process Simulation Center, California Institute of Technology, Pasadena, CA 91125; and [b]Joint Center for Artificial Photosynthesis, California Institute of Technology, Pasadena, CA 91125

Contributed by William A. Goddard III, April 14, 2018 (sent for review December 18, 2017; reviewed by Daniel G. Nocera and Annabella Selloni)

The oxygen evolution reaction (OER) is critical to solar production of fuels, but the reaction mechanism underlying the performance for a best OER catalyst, Fe-doped NiOOH [(Ni,Fe)OOH], remains highly controversial. We used grand canonical quantum mechanics to predict the OER mechanisms including kinetics and thus overpotentials as a function of Fe content in (Ni,Fe)OOH catalysts. We find that density functional theory (DFT) without exact exchange predicts that addition of Fe does not reduce the overpotential much. However, DFT with exact exchange predicts dramatic improvement in performance for (Ni,Fe)OOH, leading to an overpotential of 0.42 V and a Tafel slope of 23 mV/decade (dec), in good agreement with experiments, 0.3–0.4 V and 30 mV/dec. We reveal that the high spin d^4 Fe(IV) leads to efficient formation of an active O radical intermediate, while the closed shell d^6 Ni(IV) catalyzes the subsequent O–O coupling, and thus it is the synergy between Fe and Ni that delivers the optimal performance for OER.

density functional theory | B3PW91 | PBE | electrocatalysis | reaction mechanism

Artificial photosynthesis (AP) using solar energy to convert CO_2 and H_2O into fuels and O_2 is a most promising approach to a carbon-neutral cycle and scalable energy storage (1, 2). Electrocatalysis provides an attractive candidate route to AP, which could extend to all intermittent renewable energy resources. Another key advantage is the decomposition of AP reaction into two electrochemical half-reactions, CO_2 reduction reaction (CO_2RR) and oxygen evolution reaction (OER), that can use drastically different catalysts for optimal performance.

The rational design toward ideal electrocatalysts requires atomistic understanding of the reaction mechanisms for the target electrochemical reactions. Here, modern quantum mechanics (QM) methods can play an essential role. Indeed, the atomistic mechanisms underlying CO_2RR catalyzed by Cu and Cu-derived electrodes have been elucidated recently by using new methods of QM, including grand canonical (GC; constant electrochemical potential) QM and QM-based free energy sampling by metadynamics with full solvent, providing guidelines for efficient and selective catalyst design (3–7). However, such QM calculations of the mechanisms for OER, including reaction barriers and accurate solvent corrections, have only been reported for IrO_2 (110) (8), which is complicated by difficulties in common density functional theory (DFT) methods in describing the spin triplet O_2 product.

In this work, we examine the OER mechanism for a most efficient electrocatalyst under alkaline conditions (9), the Fe-doped NiOOH [(Ni,Fe)OOH], which remains elusive, and even the catalytic active site (Ni or Fe) is under debate (10–12). Here, we apply a state-of-the-art theoretical method, using the hybrid functional B3PW91 (13) and explicit constant electrochemical potential (μ_e) calculations (14, 15), to determine the atomistic mechanisms for OER on pure and Fe-doped NiOOH, including the kinetics of O–O coupling and O_2 release. We find that the efficiency of OER is dictated by two elementary steps, the formation of an active O radical species and the subsequent O–O coupling. However, the pure Ni system is inefficient for generating the O radical. We find that in the (Ni,Fe)OOH systems, the surface high spin d^4 Fe(IV) site delivers the O radical more easily, while it is still the surface closed shell d^6 Ni(IV) site that better catalyzes the O–O coupling. Thus, it is the synergy between Fe and Ni that offers the optimal performance of (Ni,Fe)OOH for catalyzing OER. This implies promising directions for further optimization toward ideal OER catalyst.

Results and Discussion

Composing the Appropriate Methodology. Previous theoretical efforts to model the mechanism for OER on (Ni,Fe)OOH suffer several inadequacies. First, the Ni/Fe oxide/hydroxide systems feature localized unpaired spins that demand theory beyond the standard density functional approximations [local density approximation and generalized gradient approximation (GGA)]. A commonly used strategy for remedying this is to introduce the on-site Coulomb interaction (+U) (10, 16–18), but it is questionable for modeling chemistry, because the U term generally varies as functions of the electronic configurations of transition metal (TM) atoms (19, 20). Indeed, GGA(PBE)+U has been shown to be unreliable for predicting redox potentials of Ni/Fe oxyhydroxides (12).

A more general approach is including the Hartree–Fock exchange as in the hybrid functional methods to describe the localized electrons self-consistently (13, 21), and a recent study

Significance

The oxygen evolution reaction (OER) is a key component to applications of electrochemistry in energy and environment, but the reaction mechanism for OER on a best-performing catalyst, the Fe-doped NiOOH [(Ni,Fe)OOH], is under debate. Using advanced quantum mechanics (QM) methods, we find that the (Ni,Fe)OOH systems feature synergy between Fe and Ni, in which the two components assume the two different key functionalities needed for OER, forming an active O radical and catalyzing the O–O coupling, respectively. It is this synergy that delivers the optimal performance of (Ni,Fe)OOH for driving the OER. This suggests a strategy to further improve the (Ni,Fe)OOH-type OER catalysts, i.e., separately screening for the best component for each key functionality.

Author contributions: H.X. and W.A.G. designed research; H.X. and H.S. performed research; H.X. and H.S. analyzed data; and H.X. and W.A.G. wrote the paper.

Reviewers: D.G.N., Harvard University; and A.S., Princeton University.

The authors declare no conflict of interest.

[1]To whom correspondence should be addressed. Email: wag@wag.caltech.edu.

This article contains supporting information online at www.pnas.org/lookup/suppl/doi:10.1073/pnas.1722034115/-/DCSupplemental.

Published online May 21, 2018.

of (Ni,Fe)OOH did use one of the flavors (PBE0), but focused on only the bulk phases (12).

Second, previous theoretical studies examined only the thermodynamics of intermediates for OER on (Ni,Fe)OOH, with no consideration of reaction kinetics [transition states (TSs) and associated barriers] (10, 18). Such disregard could be reasonable for the OER steps involving simple deprotonation processes associated with electrochemical oxidation, which are probably fast with barriers of a few kilocalories per mole as the proton transfer in aqueous electrolytes. But the key catalytic step before the final O_2 production is O–O coupling that is likely to have a significant barrier. Indeed, our recent study of O–O coupling during OER on IrO_2 found moderate barriers of 0.5–0.6 eV (8). Thus, to investigate the reaction kinetics for OER reactions, we can expect that exact exchange is required for predicting the kinetics accurately enough to predict reliable current densities and hence overpotentials for comparison with experiments.

Another important aspect of our calculations compared with previous theoretical modeling is our implementation of GC DFT (15) using the accurate CANDLE implicit electrolyte model (14). This allows us to describe the kinetic processes as a function of explicit μ_e in describing electrochemistry at the interface; this success was previously demonstrated for CO_2RR on Cu(111) (3, 4, 7) and OER on IrO_2(110) (8). This is in contrast to the standard QM methods in which the number of electrons is kept fixed during the reactions, leading necessarily to changes in the applied potential (U).

Here, we calculate the relative free energies by combining several components: (*i*) the internal energies from the hybrid functional B3PW91 calculations using the PBE optimized structures; (*ii*) the zero-point energies, enthalpy, and entropy contributions from PBE calculations; (*iii*) the solvation energies; and (*iv*) the explicit dependence on the U (U is referenced to the standard hydrogen electrode) calculated with PBE. *SI Appendix, SI Methods* provides the details. Note that the free energies and barriers mentioned below depend on U.

The Structural Model for the Active (Ni,Fe)OOH Catalyst. The OER active phase of (Ni,Fe)OOH systems has been identified as γ-NiOOH-like with a mixed formal oxidation state (FOS) of +3.6 for TM elements (10, 12, 22). Thus, to model the OER active phase, we use a model crystal structure (Fig. 1*A*) proposed by Ceder and coworkers based on theoretical analysis (23). This model consists of 2D (Ni,Fe)O_2 layers intercalating with H_2O molecules and K^+ ions that result in an interplanar spacing of 6.8 Å. This matches well the current knowledge of γ-phase TM oxyhydroxides (9). The model structure assumes the chemical formula of $K_{1/3}(H_2O)_{2/3}$(Ni,Fe)O_2, which gives the proper average FOS of +3.67 for Ni/Fe.

Using the magnetic moment analysis suggested by Hammes-Schiffer and coworkers to determine the FOS of each TM atom (12), our DFT calculations at the B3PW91 level predict that, for the pure Ni case, the Ni atoms closest to K^+ are of +3 FOS with a low spin d^7 configuration, while the remaining 2/3 of the Ni atoms are of +4 FOS with a closed shell d^6 configuration (Fig. 1*A*).

Introducing the Fe dopant, we find that, it preferably substitutes at the Ni^{4+} site as Fe^{4+} with a high spin d^4 configuration. This is consistent with previous experimental (Stahl and coworkers) (24) and theoretical (Hammes-Schiffer and coworkers) (12) confirmation that Fe^{4+} is present as the onset of OER activity. *SI Appendix, SI Additional Discussions* provides additional discussion of Fe doping in NiOOH.

We consider the (100) surface of the adopted model structure that exposes the nonpolar edge of the (Ni,Fe)O_2 layer (Fig. 1*B*), which has been shown by Bell and coworkers and Cui and coworkers to be the highly OER active surface in similar systems (25, 26). This surface has three TM sites per layer, of which two are of +4 FOS and the other one is of +3 FOS. Letting the pristine surface of the pure Ni case come into contact with the electrolyte, we predict that the two Ni^{4+} sites react with H_2O ($^*H_2O$) molecules chemically with one dissociated over the bridging O (O_b) and neighboring Ni^{4+} site, while the Ni^{3+} site repels the H_2O molecule due to the unpaired electron. This is shown in Fig. 1 *C* and *D*.

As described in *Composing the Appropriate Methodology*, we use the CANDLE implicit model (14) to describe the electrolyte. Thus, we introduce explicit H_2O molecules only when they chemically bind to the surface or become directly involved in the OER (The details of these structures are provided in *SI Appendix, SI Structural Information: Coordinates for All Predicted Intermediates and Transition States*).

The Reaction Pathway for OER on the Pure Ni System. To determine the reaction pathway for OER on the pure Ni system, we examine every possible option for deprotonation associated with each electrochemical oxidation step (losing one electron) to find the lowest free energy state.

a. The four electron steps for the pure Ni case (Fig. 2*A*)
0. We start with state 1 with 2/3 H_2O coverage,

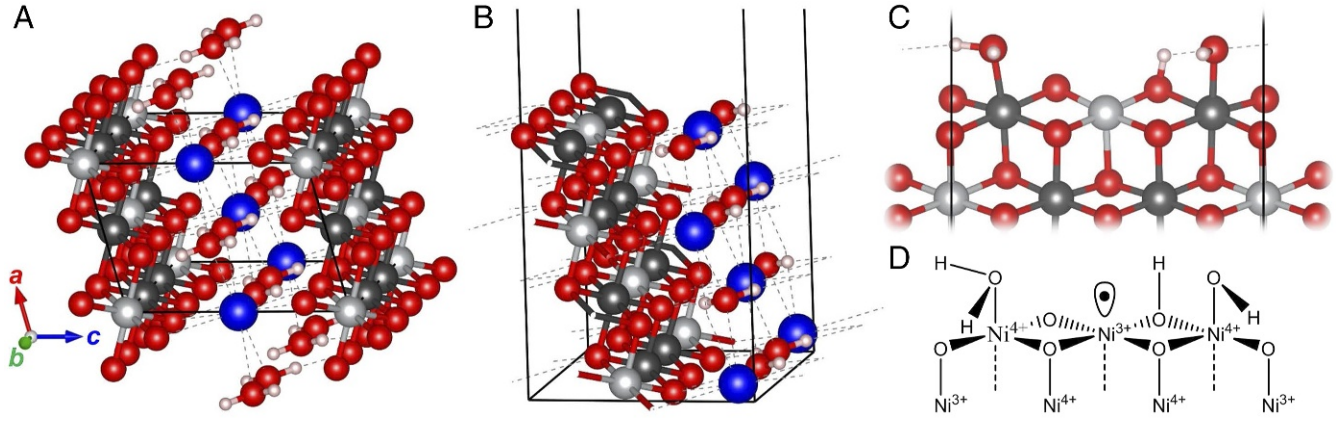

Fig. 1. Structural models for the OER active (Ni,Fe)OOH catalysts. (*A*) The model crystal structure for the OER active γ-phase of (Ni,Fe)OOH catalysts, with chemical formula $K_{1/3}(H_2O)_{2/3}$(Ni,Fe)O_2 [light gray for Ni^{3+}, dark gray for $(Ni,Fe)^{4+}$, blue for K^+, red for O, and white for H]. (*B*) The highly OER active (100) surface of *A*. (*C*) The configuration of water chemisorption on the active surface of the pure Ni system. (*D*) The chemical illustration corresponding to *C*. Note that the intercalating K^+ and H_2O are omitted for clarity in *C* and *D*.

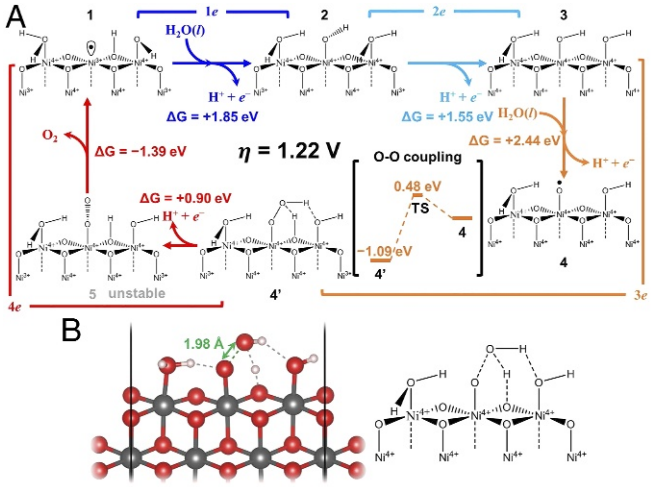

Fig. 2. Mechanism for OER on pure γ-NiOOH catalyst. (*A*) The mechanistic cycle of OER catalyzed by pure γ-NiOOH surface [B3PW91 predicted free energy differences ΔG and barrier at U = 2.28 V (η = 1.22 V) corresponding to j = 10 mA/cm^2]. (*B*) The structure of TS for O–O coupling.

1. then the first electron ($1e$) step features deprotonating the O_b while bringing in a third H_2O to hydroxylate Ni^{4+} that is oxidized from the Ni^{3+} site. This results in state 2 with 1/3 OH coverage and 2/3 H_2O coverage.
2. Instead of further deprotonating the adsorbed OH (*OH) to a presumably active O species, we find that the second electron ($2e$) step favors deprotonating one $^*H_2O$ to produce state 3 with 2/3 OH coverage.
3. It is the third electron ($3e$) step that generates a stable O species as in state 4, requiring a large free energy input of ~2.4 eV. This O species is predicted to be a radical by both PBE and B3PW91 calculations, which give spin populations on O of 0.6 and 1.0, respectively. Thus, we identify by theory that the nature of the active O species is an O radical, consistent with previous experiments (22, 27–31). Consequently, we find that the closed shell d^6 Ni^{4+} is ineffective in producing this key active intermediate. We find that the alternative pathway through Ni(III)-O• is unfavorable (*SI Appendix, SI Additional Discussions*).
   Interestingly, state 4 is not the most stable at the $3e$ step, but when a fourth H_2O is introduced, we find that state 4′ with an adsorbed OOH (*OOH) and hydrogenated O_b is lower in free energy by 0.7–1.1 eV. Our B3PW91 calculations predict a moderate free energy barrier of 0.5–0.6 eV going from state 4 to 4′. This TS features simultaneous O–O bond forming and protonating O_b by the incoming H_2O (Fig. 2*B*). The O–O coupling within the $3e$ step does not involve losing any electron and thus is not an electrochemical step but a chemical one.
   We note that there have been two prevailing mechanisms for O–O coupling in OER on TM oxo complexes, the water hydrogen atom abstraction (WHAA) mechanism and the intramolecular oxygen coupling (IMOC) mechanism (31, 32). Our mechanism resembles the WHAA mechanism, but differs significantly in the aspect that the WHAA mechanism involves two O radicals for O–O coupling and H abstraction from H_2O, respectively, but our mechanism involves only one O radical, and the O_b abstracts the H atom from H_2O.
4. After the state 4′ is formed, the fourth electron ($4e$) step deprotonates the *OOH, leading to state 5. Although PBE predicts a free energy barrier of ~0.4 eV for state 5 to release O_2 and recover the original state 1, B3PW91 finds a barrierless downhill reaction, indicating an unstable state 5 and thus immediate O_2 release after *OOH deprotonation. This drives state 4′ back to state 1. Thus, the $4e$ step completes the OER cycle.

b. Calculating the current density (j) vs. U

Having elucidated the four electron steps and the associated energetics (including barriers), we can now compute the current density (j) at any U. We use a microkinetic model assuming the steady-state approximation (more details are in *SI Appendix, SI Methods*). Thus, we solve numerically for the onset potential U_{on} at which the U-dependent free energies and barriers deliver a j of 10 mA/cm^2. To calculate the overpotential $\eta = U_{on} - U_0$, we use the equilibrium potential U_0 of OER predicted by the corresponding level of theory (1.06 V by B3PW91, 1.13 V by PBE) for consistency. Both B3PW91 and PBE predict a much larger η of 1.22 and 0.97 V, respectively, than the experimental value of 0.7 V for OER on pure γ-NiOOH (10). This leads us to consider the role of Fe impurities. Indeed, some experimental studies have pointed out that it is very likely that preparation of NiOOH catalysts may easily have introduced Fe impurities accidentally (33).

The Reaction Pathway of OER for 1/3 Fe on the Top Surface. We first consider a single Fe dopant atom replacing one of the 12 Ni atoms among the four layers in our model. We find that this Fe very strongly prefers to substitute the surface Ni^{4+} site that has the *OH (Fig. 3*A*, state 1). It is 0.4–0.5 eV higher in energy to move this Fe into subsurface Ni sites, making it likely that for small concentrations of Fe, all are at the surface. Indeed, even with trace amounts of Fe impurities, the surface Fe concentration may possibly reach as high as the fraction 1/3 considered here.

With the presence of 1/3 surface Fe doping in γ-NiOOH, we find a dramatic change in the OER mechanism (Fig. 3*A*). The key change is that the formation of active O radical is moved to the $2e$ step, and the O radical is now bonded to the surface

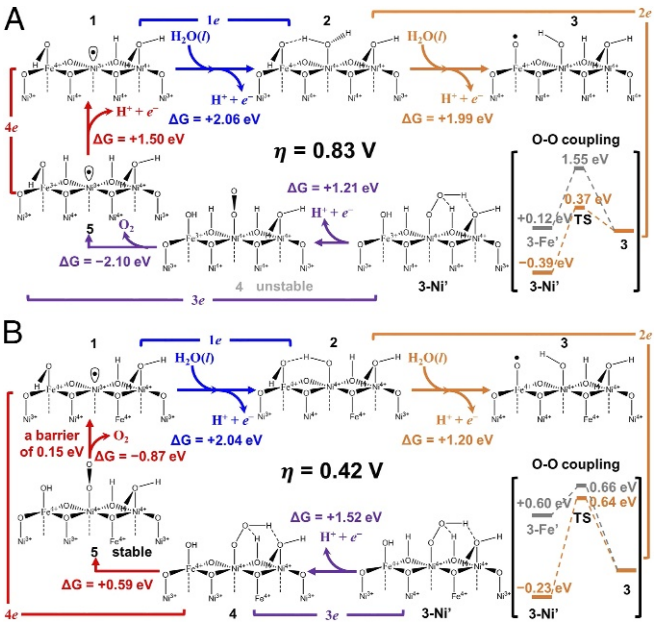

Fig. 3. The mechanistic cycles for OER on γ-(Ni,Fe)OOH catalysts (based on B3PW91 predicted free energies and barriers). (*A*) One-third surface Fe doping case, leading to U = 1.89 V (η = 0.83 V) for j = 10 mA/cm^2. (*B*) One-third surface Fe doping plus 1/3 subsurface Fe doping, leading to U = 1.48 V (η = 0.42 V) for j = 10 mA/cm^2.

Fe^{4+} site. The high spin d^4 configuration of the Fe^{4+} site provides great stabilization for the unpaired electron on O radical through exchange interactions, reducing the free energy cost to 1.9–2.0 eV rather than ∼2.4 eV. We find that the possible alternative pathway through Fe(III)-O• is unfavorable (*SI Appendix, SI Additional Discussions*).

However, we find that the subsequent O–O coupling within the $2e$ step still takes place on the surface Ni^{4+} site (originally Ni^{3+}). This is favored by both kinetics (a barrier of ∼0.4 eV) and thermodynamics (downhill by 0.2–0.4 eV). It requires a much larger barrier of ∼1.6 eV to catalyze the O–O coupling on the surface Fe^{4+} site, and the resulting *OOH bonded to Fe^{4+} is even higher in free energy by 0.1–0.3 eV than the O radical state. This indicates that thermodynamically this Fe^{4+}-*OOH state is not viable at the $2e$ step.

The subsequent $3e$ step after formation of *OOH on Ni^{4+} (state 3-Ni′) is similar to the pure Ni case, which exhibits simultaneous *OOH deprotonation and O_2 release, to proceed directly to state 5 (Fig. 3*A*).

The final $4e$ step is then a simple deprotonation of Ob to recover the starting surface.

Our OER mechanism for surface-doped Fe on γ-NiOOH is characterized by Fe-catalyzed O radical generation and Ni-catalyzed O–O coupling. This is predicted by B3PW91 to have an η of 0.83 V, which is close to the experimental value of 0.7 V for OER on pure γ-NiOOH (10). This provides further evidence to support the conclusion that the observed performance for pure NiOOH catalyst may be strongly affected by Fe impurities.

The Reaction Pathway of OER for 1/3 Fe on the Top Surface and 1/3 Fe at the Subsurface Layer. We next consider two Fe dopant atoms distributed among the 12 Ni sites. We find that the second Fe favors substituting at the subsurface Ni^{4+} site (Fig. 3*B*, state 1) over populating further the surface sites by ∼0.1 eV in energy. This implies that extra Fe doping does not increase the surface Fe concentration to >1/3, but instead pushes Fe substitution into subsurface regions.

Thus, our model with two Fe dopant atoms forms a basis to understand the intentional Fe doping that leads to optimal performance. With the presence of subsurface Fe in addition to surface Fe, the OER mechanism remains similar (Fig. 3*B*) to that for the surface Fe-only case, but the energetics are modified significantly. Particularly, the free energy input required for O radical formation is reduced drastically from 1.9–2.0 eV to only 1.2–1.3 eV, while the barrier for O–O coupling increases slightly from ∼0.4 to 0.5–0.6 eV. This combination leads to an η of 0.42 V, which is very close to the experimental value of 0.3–0.4 V for the best-performing (Ni,Fe)OOH catalysts (10, 34, 35). Thus, we believe that our model likely captures the essence for optimal performance of (Ni,Fe)OOH catalysts.

An interesting result from these calculations is that the (Ni,Fe)OOH catalyst is bifunctional: With both Ni and Fe providing core functionalities for driving the OER,

- The surface Fe(IV) site with a high spin d^4 configuration stabilizes the key active O radical intermediate,
- While the surface Ni(IV) site with its closed shell d^6 configuration takes charge of catalyzing the O–O coupling that is a key step toward the O_2 product.

Thus, it is the synergy between Fe and Ni that delivers the optimal performance of (Ni,Fe)OOH for catalyzing the OER. A second feature for the case with two Fe dopant atoms is that the superoxide ($^*O_2$) intermediate on Ni is stabilized by a small free energy barrier of 0.1–0.2 eV. Indeed, experiments have shown spectroscopic evidence for the existence of an active NiOO species (36). This strongly supports our conclusion that (Ni,Fe)OOH is a bifunctional OER catalyst. This conclusion suggests that the performance of (Ni,Fe)OOH-like catalysts might be further optimized through independently searching for better candidate TMs to stabilize the O radical and to catalyze the O–O coupling. Such catalysts might be synthesized by combining them via techniques such as the sol-gel method (37).

We note that the IMOC mechanism has been suggested for OER on Co–OEC complexes (31). On the γ-(Ni,Fe)OOH catalysts considered here, it requires a large free energy input of >2.4 eV to form a second neighboring O radical on Ni site that is necessary to drive the IMOC mechanism. In contrast, our mechanism is favored by a free energy downhill of 0.2 eV through reacting the O radical with H_2O, with overcoming a barrier of only 0.6 eV. Thus, our results indicate that the IMOC mechanism is not favored for OER on the γ-(Ni,Fe)OOH catalysts.

For the optimal (Fe,Ni)OOH catalyst, B3PW91 predicts a Tafel slope of 23 mV/decade (dec) (Fig. S4), comparable to the experimental value of 30 mV/dec (38, 39). The deviation of 7 mV/dec suggests an underestimation of the barrier for O–O coupling by 0.1 eV.

The Turnover Limiting Step. Experiments have found a sharp distinction between Tafel slopes for OER on pure NiOOH compared with the optimal (Fe,Ni)OOH catalyst:

- Tafel slopes of 90−120 and 70 mV/dec have been reported for OER on the pure NiOOH in KB_i (pH 9.2) (39, 40) and 5.5 M KOH (38) electrolytes, respectively, implying an electron transfer step as the turnover limiting step (TLS). This scenario is similar to the hydrogen evolution reaction (HER) with the Volmer step being the TLS.
- A Tafel slope of 30 mV/dec has been reported for OER on the optimal (Fe,Ni)OOH catalyst in both KB_i (39) and 1 M KOH (38) electrolytes, indicating a two-electron transfer before a chemical TLS. This scenario is similar to HER with the Tafel step being the TLS.

Our mechanism is quite consistent with both experiments. On the optimal (Fe,Ni)OOH catalyst (Fig. 3*B*), the O radical is stabilized by Fe and thus easily formed, so that the step from state 1 to 2 becomes the most energy-consuming, which results in state 1 becoming the resting state at the OER operating potentials predicted by our microkinetic simulation. Our calculated Tafel slope of 23 mV/dec indicates that the TLS for OER on the optimal (Fe,Ni)OOH catalyst is the chemical O–O coupling step after two electron transfer steps from the resting state. As discussed above, the deviation of 7 mV/dec may imply an underestimation of barrier for O–O coupling by 0.1 eV.

On the other hand, for the pure NiOOH (Fig. 2*A*), the step from state 3 to 4 (the state with the O radical) is the most energy-consuming, and this results in state 3 becoming the resting state (the most populous state) at the OER operating potentials predicted by our microkinetic simulation. Since our

Table 1. Comparison of predicted η's for OER on (Ni,Fe)OOH catalysts

Methods	η (V) at 10 mA/cm^2 for different surface Fe concentration C[Fe$_s$] and below surface (considered as bulk) Fe concentration C[Fe$_b$]		
	C[Fe$_s$] = 0, C[Fe$_b$] = 0	C[Fe$_s$] = 1/3, C[Fe$_b$] = 0	C[Fe$_s$] = 1/3, C[Fe$_b$] = 1/9*
Expt.	0.7 (ref. 10)	0.7 (ref. 10)	0.3–0.4 (refs. 10, 34, and 35)
B3PW91	1.22	0.83	0.42
PBE	0.97	0.88	0.79

Expt., experiment.

*Note that here the 1/3 subsurface Fe doping is converted to C[Fe$_b$] by including the bottom two pure Ni layers, which might not correspond to the realistic C[Fe$_b$], as the deeper bulk region (beyond the four-layer slab model we considered) might contain more Fe doping.

calculated Tafel slope of 61 mV/dec differs from the experiments (90−120 mV/dec), we conclude that the TLS for OER on the pure NiOOH is the chemical O–O coupling step after one reversible electron transfer step that generates the O radical right from the resting state. This scenario is similar to OER on the Co–Pi catalyst (28). The discrepancy between our prediction and experiments might arise from our assumption that the electron transfer is fast and not rate-limiting, while the experimental Tafel slopes of 90−120 mV/dec for OER on the pure NiOOH indicates an electron transfer step as the TLS.

Therefore, in addition to the synergy between Ni and Fe, the stabilization of O radical by Fe plays a second essential role in shifting the TLS to become the chemical O–O coupling preceded by two electron transfer steps, which leads to the much lower calculated Tafel slope of 23 mV/dec. This in turn allows only a small increase in applied potential to substantially increase the current.

PBE vs. B3PW91 Flavor of DFT. Our preceding discussion used the results from the B3PW91 flavor of DFT. This is because it is well known that such hybrid methods often lead to much more accurate results than PBE. We also carried out PBE calculations for all of the steps discussed for B3PW91. Table 1 summarizes the predicted η's by B3PW91 and PBE for the pure and Fe-doped γ-NiOOH. Most interesting here is that PBE predicts that Fe doping leads to only slight improvement of OER performance, changing from $\eta = 0.97$ to 0.88–0.79 V for the cases in which 0, 1, and 2 of the 12 Ni are replaced with Fe. Thus, for OER, PBE leads to direct contradiction to experiment. In contrast, B3PW91 leads to $\eta = 1.22$ to 0.83 to 0.42 V for the cases in which 0, 1, and 2 of the 12 Ni are replaced with Fe. Thus, B3PW91 is quite consistent with the dramatic improvement in performance observed experimentally. This highlights the necessity for using hybrid functional methods to describe chemistry on catalysts with localized electrons/spins.

Summary

Using advanced QM methods (hybrid DFT and GC-QM), we determined the atomistic mechanisms including the kinetics of O–O coupling for OER on pure and Fe-doped NiOOH catalysts. We discovered two key steps of OER:

- The formation of an active O radical species; and
- The subsequent O–O coupling.

Our results find that the pure NiOOH is a poor OER catalyst, because it is ineffective at producing the O radical. In contrast, the (Ni,Fe)OOH systems feature synergy between Fe and Ni: The high spin d^4 Fe(IV) stabilizes the O radical by exchange interaction to generate it efficiently, while the closed shell d^6 Ni(IV) catalyzes the O–O coupling. Thus, the two components assume the two different key functionalities needed for OER. It is this synergy that delivers the optimal performance of (Ni,Fe)OOH for driving the OER. Moreover, the stabilization of O radical by Fe plays an essential role in shifting the TLS to be the chemical O–O coupling preceded by two electron transfer steps, which leads to a much lower Tafel slope. This suggests that the (Ni,Fe)OOH-type OER catalysts might be improved further by separately screening for the best component for each key functionality.

ACKNOWLEDGMENTS. This work was supported by the Joint Center for Artificial Photosynthesis, a Department of Energy (DOE) Energy Innovation Hub, supported through the Office of Science of the DOE under Award DE-SC0004993. The calculations were carried out on the Extreme Science and Engineering Discovery Environment, which is supported by National Science Foundation Grant ACI-1053575, and the Zwicky Astrophysics Supercomputer at Caltech.

1. Lewis NS, Nocera DG (2006) Powering the planet: Chemical challenges in solar energy utilization. *Proc Natl Acad Sci USA* 103:15729–15735.
2. Lewis NS (2016) Developing a scalable artificial photosynthesis technology through nanomaterials by design. *Nat Nanotech* 11:1010–1019.
3. Xiao H, Cheng T, Goddard WA, Sundararaman R (2016) Mechanistic explanation of the pH dependence and onset potentials for hydrocarbon products from electrochemical reduction of CO on Cu(111). *J Am Chem Soc* 138:483–486.
4. Xiao H, Cheng T, Goddard WA (2017) Atomistic mechanisms underlying selectivities in C_1 and C_2 products from electrochemical reduction of CO on Cu(111). *J Am Chem Soc* 139:130–136.
5. Cheng T, Xiao H, Goddard WA (2016) Reaction mechanisms for the electrochemical reduction of CO_2 to CO and formate on the Cu(100) surface at 298 K from quantum mechanics free energy calculations with explicit water. *J Am Chem Soc* 138:13802–13805.
6. Cheng T, Xiao H, Goddard WA (2017) Full atomistic reaction mechanism with kinetics for CO reduction on Cu(100) from ab initio molecular dynamics free-energy calculations at 298 K. *Proc Natl Acad Sci USA* 114:1795–1800.
7. Xiao H, Goddard WA, Cheng T, Liu Y (2017) Cu metal embedded in oxidized matrix catalyst to promote CO_2 activation and CO dimerization for electrochemical reduction of CO_2. *Proc Natl Acad Sci USA* 114:6685–6688.
8. Ping Y, Nielsen RJ, Goddard WA (2017) The reaction mechanism with free energy barriers at constant potentials for the oxygen evolution reaction at the IrO_2(110) surface. *J Am Chem Soc* 139:149–155.
9. Suen NT, et al. (2017) Electrocatalysis for the oxygen evolution reaction: Recent development and future perspectives. *Chem Soc Rev* 46:337–365.
10. Friebel D, et al. (2015) Identification of highly active Fe sites in (Ni,Fe)OOH for electrocatalytic water splitting. *J Am Chem Soc* 137:1305–1313.
11. Li N, et al. (2017) Influence of iron doping on tetravalent nickel content in catalytic oxygen evolving films. *Proc Natl Acad Sci USA* 114:1486–1491.
12. Goldsmith ZK, et al. (2017) Characterization of NiFe oxyhydroxide electrocatalysts by integrated electronic structure calculations and spectroelectrochemistry. *Proc Natl Acad Sci USA* 114:3050–3055.
13. Becke AD (1993) Density-functional thermochemistry. III. The role of exact exchange. *J Chem Phys* 98:5648–5652.
14. Sundararaman R, Goddard WA (2015) The charge-asymmetric nonlocally determined local-electric (CANDLE) solvation model. *J Chem Phys* 142:064107.
15. Sundararaman R, Goddard WA, Arias TA (2017) Grand canonical electronic density-functional theory: Algorithms and applications to electrochemistry. *J Chem Phys* 146:114104.
16. García-Mota M, et al. (2012) Importance of correlation in determining electrocatalytic oxygen evolution activity on cobalt oxides. *J Phys Chem C* 116:21077–21082.
17. Liao P, Keith JA, Carter EA (2012) Water oxidation on pure and doped hematite (0001) surfaces: Prediction of Co and Ni as effective dopants for electrocatalysis. *J Am Chem Soc* 134:13296–13309.
18. Li YF, Selloni A (2014) Mechanism and activity of water oxidation on selected surfaces of pure and Fe-doped niox. *ACS Catal* 4:1148–1153.
19. Cococcioni M, de Gironcoli S (2005) Linear response approach to the calculation of the effective interaction parameters in the lda+u method. *Phys Rev B* 71:035105.
20. Kulik HJ, Cococcioni M, Scherlis DA, Marzari N (2006) Density functional theory in transition-metal chemistry: A self-consistent Hubbard U approach. *Phys Rev Lett* 97:103001.
21. Cohen AJ, Mori-Sánchez P, Yang W (2008) Insights into current limitations of density functional theory. *Science* 321:792–794.
22. Bediako DK, et al. (2012) Structure-activity correlations in a nickel-borate oxygen evolution catalyst. *J Am Chem Soc* 134:6801–6809.
23. Van der Ven A, Morgan D, Meng YS, Ceder G (2006) Phase stability of nickel hydroxides and oxyhydroxides. *J Electrochem Soc* 153:A210–A215.
24. Chen JYC, et al. (2015) Operando analysis of NiFe and Fe oxyhydroxide electrocatalysts for water oxidation: Detection of Fe^{4+} by Mössbauer spectroscopy. *J Am Chem Soc* 137:15090–15093.
25. Bajdich M, García-Mota M, Vojvodic A, Nørskov JK, Bell AT (2013) Theoretical investigation of the activity of cobalt oxides for the electrochemical oxidation of water. *J Am Chem Soc* 135:13521–13530.
26. Lu Z, et al. (2017) Identifying the active surfaces of electrochemically tuned $LiCoO_2$ for oxygen evolution reaction. *J Am Chem Soc* 139:6270–6276.
27. Kanan MW, et al. (2010) Structure and valency of a cobalt-phosphate water oxidation catalyst determined by in situ X-ray spectroscopy. *J Am Chem Soc* 132:13692–13701.
28. Surendranath Y, Kanan MW, Nocera DG (2010) Mechanistic studies of the oxygen evolution reaction by a cobalt-phosphate catalyst at neutral pH. *J Am Chem Soc* 132:16501–16509.
29. Bediako DK, Surendranath Y, Nocera DG (2013) Mechanistic studies of the oxygen evolution reaction mediated by a nickel-borate thin film electrocatalyst. *J Am Chem Soc* 135:3662–3674.
30. Bediako DK, Costentin C, Jones EC, Nocera DG, Savéant JM (2013) Proton-electron transport and transfer in electrocatalytic films. Application to a cobalt-based O_2-evolution catalyst. *J Am Chem Soc* 135:10492–10502.
31. Ullman AM, Brodsky CN, Li N, Zheng SL, Nocera DG (2016) Probing edge site reactivity of oxidic cobalt water oxidation catalysts. *J Am Chem Soc* 138:4229–4236.
32. Betley TA, Wu Q, Van Voorhis T, Nocera DG (2008) Electronic design criteria for O-O bond formation via metal-oxo complexes. *Inorg Chem* 47:1849–1861.
33. Trotochaud L, Young SL, Ranney JK, Boettcher SW (2014) Nickel-iron oxyhydroxide oxygen-evolution electrocatalysts: The role of intentional and incidental iron incorporation. *J Am Chem Soc* 136:6744–6753.

34. McCrory CCL, Jung S, Peters JC, Jaramillo TF (2013) Benchmarking heterogeneous electrocatalysts for the oxygen evolution reaction. *J Am Chem Soc* 135:16977–16987.
35. Song F, Hu X (2014) Exfoliation of layered double hydroxides for enhanced oxygen evolution catalysis. *Nat Commun* 5:4477.
36. Trześniewski BJ, et al. (2015) In situ observation of active oxygen species in Fe-containing Ni-based oxygen evolution catalysts: The effect of pH on electrochemical activity. *J Am Chem Soc* 137:15112–15121.
37. Zhang B, et al. (2016) Homogeneously dispersed multimetal oxygen-evolving catalysts. *Science* 352:333–337.
38. Corrigan DA (1987) The catalysis of the oxygen evolution reaction by iron impurities in thin film nickel oxide electrodes. *J Electrochem Soc* 134:377–384.
39. Dincă M, Surendranath Y, Nocera DG (2010) Nickel-borate oxygen-evolving catalyst that functions under benign conditions. *Proc Natl Acad Sci USA* 107:10337–10341.
40. Smith AM, Trotochaud L, Burke MS, Boettcher SW (2015) Contributions to activity enhancement via Fe incorporation in Ni-(oxy)hydroxide/borate catalysts for near-neutral pH oxygen evolution. *Chem Commun* 51:5261–5263.